MIGRATION AND TOMOGRAPHIC IMAGING OF COLLUVIAL WEDGES AND FAULTS OVER THE WASHINGTON FAULT, ARIZONA

by

Shengdong Liu

A thesis submitted to the faculty of
The University of Utah
in partial fulfillment of the requirements for the degree of

Master of Science

in

Geophysics

Department of Geology and Geophysics

The University of Utah

December 2015

The University of Utah Graduate School

STATEMENT OF THESIS APPROVAL

This thesis of   **Shengdong Liu**

has been approved by the following supervisory committee members:

Gerard T. Schuster , Chair		**11/18/2014**
		Date Approved
Richard D. Jarrard , Member		**11/18/2014**
		Date Approved
Michael S. Thorne , Member		**11/18/2014**
		Date Approved

and by   **John M. Bartley**   , Chair of

the Department of   **Geology and Geophysics**

and by David B. Kieda, Dean of The Graduate School.

ABSTRACT

Two-dimensional (2-D) and three-dimensional (3-D) seismic surveys are conducted across the Washington fault zone of northern Arizona, with the purpose of imaging the fault-related structures to a depth of 30 m by 3-D traveltime tomography and 2-D poststack migration. The scientific objective is to use the seismic methods instead of a trenching log to deduce the paleoseismic characters of this fault zone, and to guide paleoseismologists in the optimal placement of a future trenching survey. The first-arrival traveltimes of the data are picked and inverted for the P-wave velocity distribution. Tomographic results delineate two large low-velocity zones (LVZ), which are interpreted as two colluvial wedge packages. To detect the fault structures, which have more observable reflection energy than the 3-D data, the 2-D seismic data are migrated. Four faults are recovered in the migration image, including the main fault, and possible antithetic fault. The fault location is identical to that in the tomogram and raypath density image. The main fault in the tomogram is also consistent with the results from the geomorphology survey. These results demonstrate that seismic imaging methods (3-D traveltime tomography and 2-D reflection imaging) can delineate the shape and depth of LVZs associated with colluvial wedges. Although these LVZ images cannot unambiguously delineate different rupture events in a colluvial package, they can be used to optimally design a follow-on trenching survey. Combining the paleoseismic data with the fault slip inferred by tomography, the age of the fault is speculatively estimated to be younger than 16 kyr. Future work should compare my interpreted tomogram with the trench log soon to be excavated by personnel of the Utah Geological Survey (UGS), and analyze the validity of my geological interpretation. This trench was designed using the results of this survey, which is partial justification for seismic surveys over normal fault scarps.

To my family.

CONTENTS

LIST OF FIGURES

LIST OF TABLES

ACKNOWLEDGMENTS

CHAPTER 1

INTRODUCTION

A colluvial wedge is geophysically characterized as a low-velocity zone (LVZ) surrounded by alluvial deposits, where colluvial material is deposited after a surface earthquake rupture (Morey and Schuster, 1999). Various properties of buried colluvial wedges, such as their location, size, and organic content, can record the rupture history of a fault. To study the subsurface structures over a fault zone with seismic methods, several seismic surveys over the Wasatch and Oquirrh fault zones were carried out by University of Utah personnel, and the seismic data were processed with a traveltime tomography method to detect the LVZs; in addition, reflection processing was used to delineate the fault locations. Their results showed that seismic imaging techniques can provide deeper and wider, but less resolved images of faults and colluvial wedges than the standard excavation and logging of trenches across faults (Buddenseik et al., 2007; Morey and Schuster, 1999; Sheley et al., 2003). The purpose of this thesis research is to reconstruct the shallow fault structures and colluvial wedges ($0 < Z < 30$ m) along a portion of the Washington fault zone, northern Arizona, with 2-D and 3-D seismic imaging techniques. These results are used to guide the optimal placement of an excavated paleoseismic trench along the Washington fault.

The Washington fault zone lies along the western margin of the Colorado Plateau, extending northward from the Shivwits Plateau in Arizona into the St. George basin of southwestern Utah. Southwestern Utah and northwestern Arizona are within the intermountain seismic belt of North America, a tectonically active area with several faults that could generate large earthquakes. The Washington fault is a relatively active normal fault in this region, although it has not experienced any earthquakes of magnitude larger than 6.5. However, geological studies indicate that faults in the region could produce earthquakes of magnitude 7 to 7.5 (Arabasz et al., 1992), which is of strong concern to the residents of the rapidly growing population center of St. George, Utah. The most recent large earthquake was a magnitude 5.8 event in September 1992, with the epicenter located in the Washington Dome quadrangle (Pechmann et al., 1995). The Washington fault is estimated to be 10,000

-25,000 years old based on evidence from soil profiles exposed in trenches in the area west of Warner Ridge (Earth Science Associates, 1982), and the dip of the Washington fault varies from 80 degrees west to nearly vertical (Higgins, 1998).

This thesis is organized into five sections. Section 1 is the introduction and Section 2 describes details about data acquisition and processing. The third and fourth sections present the results of synthetic tests and field data processing, respectively. The final section contains the conclusions.

CHAPTER 2

SEISMIC SURVEYS AND PROCESSING METHODS

This chapter describes the acquisition parameters and geometry of the 2-D and 3-D seismic experiments conducted across the Washington fault scarp in northern Arizona. The data-processing methods (traveltime tomography, reflection stacking, and poststack migration) are briefly explained.

2.1 Seismic Surveys

2.1.1 2-D Seismic Survey

In March 2008, UTAM researchers carried out a 2-D high-resolution seismic survey perpendicular to the Washington fault scarp near the Arizona-Utah border. Figure 2.1 shows the seismic survey site and the proposed trench site. The 2-D seismic data were collected using 96 vertical-component geophones spaced 1 m apart for a total line length of 95 m. Figure 2.2 shows the source and receiver lines, and the fault strike direction. Seismic sources, using a 16-lb sledgehammer striking a small metal plate, were initiated at every second geophone and stacked five times for each hammer (i.e., shot) position to improve the signal-to-noise ratio of each record. Recording of traces was carried out with a 120-channel Bison data recorder. Table 2.1 summarizes the acquisition and source-receiver parameters of the 2-D and 3-D seismic surveys.

2.1.2 3-D Seismic Survey

A 3-D seismic survey was carried out at the same location as the 2-D survey in October 2008 in order to obtain higher-resolution images of the subsurface. The 3-D acquisition geometry consisted of six parallel lines, where there were 80 in-line receivers with a 1 m spacing near the fault scarp and a 2 m spacing far away from the fault scarp. The cross-line spacing was 1.5 m. Shots were also activated at every other geophone, and the experiment geometry is shown in Figure 2.3.
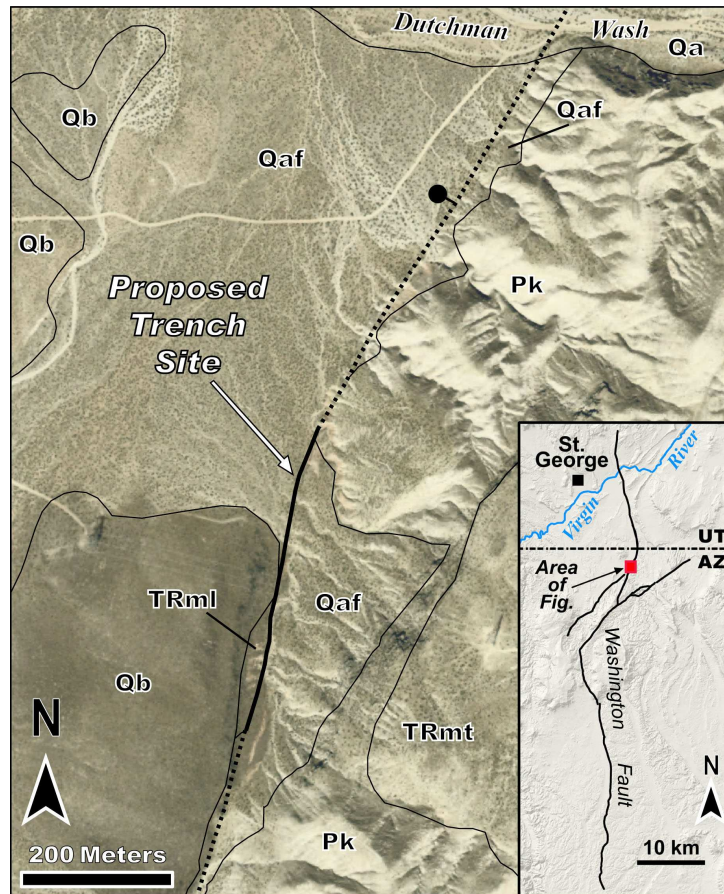
Figure 2.1. The map of the Washington fault and the survey site (provided by Utah Geological Survey). The location of the survey site is 5 km south of the Utah-Arizona border.

Figure 2.2. View of the Washington fault scarp and 2-D seismic survey line. The yellow line represents the fault strike direction, and the green line represents the 2-D seismic survey line.

Table 2.1. Parameters for the 2-D and 3-D seismic surveys.

Surveys	2-D	3-D
Sources	16-lb sledgehammer	10-lb sledgehammer
Recording instruments	one 120-channel BISON	two 120-channel BISONs
Number of shots	48	40/line (6 lines)
Number of receivers	96	80/line (6 lines)
Shot spacing	2 m	shown in Figure 2.3
Receiver spacing	1 m	shown in Figure 2.3
Survey length	95 m	119 m
Number of traces	4,608	115,200
Sampling interval	0.25 ms	0.25 ms
Record length	1.0 sec	1.0 sec
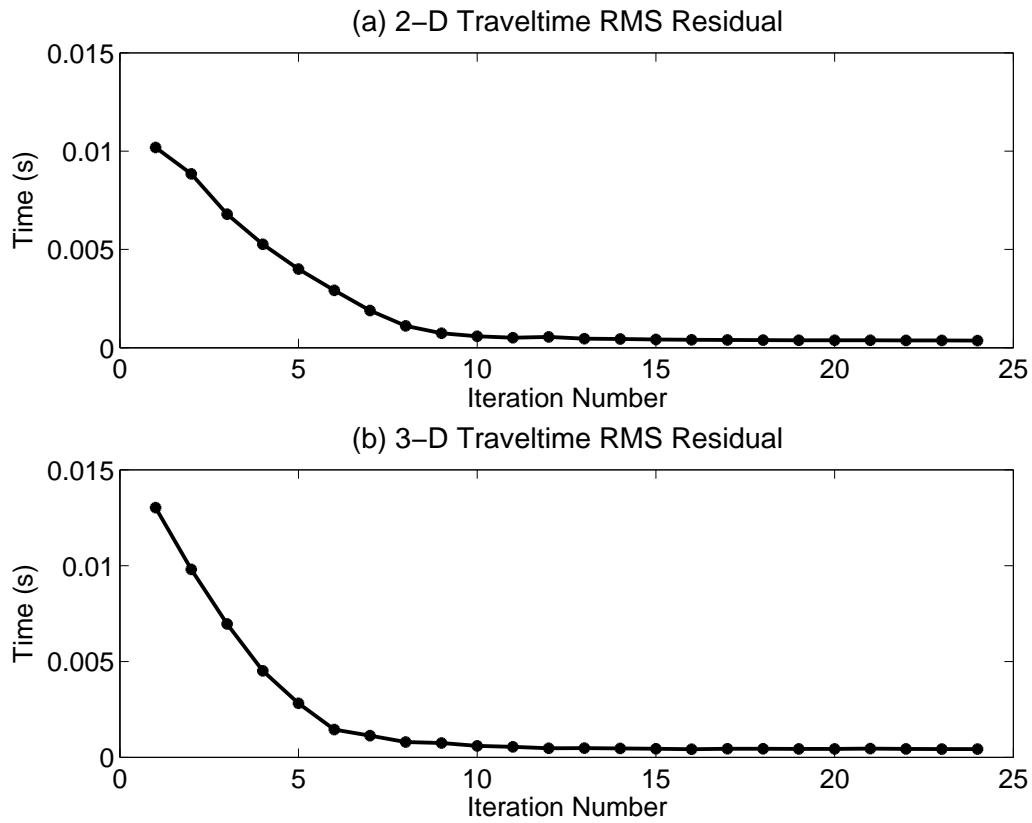
Figure 2.3. Survey geometry for the 3-D experiment. The open circles denote the locations of sources, the solid dots denote the locations of receivers, and the dashed blue line denotes the location of the fault scarp. The crossline spacing is 1.5 m, the inline spacing of coarsely spaced receivers (far from the fault scarp) is 2 m, and that of finely spaced receivers (near the fault scarp) is 1 m. The sources are activated at every other receiver.

2.2 Traveltime Tomography

2.2.1 Methodology

Traveltime tomography is a standard methodology for reconstructing the subsurface velocity distribution from first-arrival traveltimes (Aldridge and Oldenburg, 1993; Ammon and Vidale, 1993; Lutter et al., 1990; Nemeth et al., 1997; Nolet, 1987 and many others), where velocities are updated by an iterative method such as the SIRT technique (Gilbert, 1972). The tomography method consists of a number of steps. First, an initial velocity model is estimated from the x-t slope of the first-arrival in the seismograms. The traveltimes are then computed from the starting model by a finite-difference solution to the eikonal equation (Qin et al., 1992). In this case, the data misfit function can be defined as:

$$\epsilon = \frac{1}{2} \sum_i (t_i^{obs} - t_i^{cal})^2, \tag{2.1}$$

where the summation is over the i_{th} raypaths, t_i^{obs} is the associated first-arrival traveltime pick, and t_i^{cal} is the calculated traveltime. The j_{th} gradient γ_j of the misfit function is defined as:

$$\gamma_j = \frac{\delta \epsilon}{\delta s_j} = \sum_i \delta t_i \frac{\delta t_i}{\delta s_j} = \sum \delta t_i l_{ij}, \tag{2.2}$$

where δt_i is the traveltime residual, δs_j is the slowness in the jth cell and l_{ij} is the segment length of the i_{th} ray that visits the j_{th} cell. The slowness model is iteratively updated by a gradient-optimization method (i.e., steepest descent). The details of the 3-D traveltime tomography algorithm are described in the Appendix.

2.2.2 Traveltime Picking and Quality Control

The first step in tomography processing is to pick first-arrival traveltimes. Approximately 4,608 and 115,200 traveltimes are picked, respectively, from the original 2-D and 3-D Washington fault data using ProMAX software. A sample shot gather of the 2-D data with the picked first-arrival traveltime is shown in Figure 2.4.

Before computing the traveltime tomogram, a quality control of the traveltime picks is required for a reliable inversion. An important method for the quality control of traveltime picks is a reciprocity test. For traveltime pairs t_{ij} and t_{ji}, where t_{ij} represents the first-arrival traveltime pick for a source at the ith position and a receiver at the jth position, and t_{ji} represents the reciprocal traveltime pick of t_{ij}, if the reciprocity condition $t_{ij} = t_{ji}$ is not satisfied to within a tolerance of 3 milliseconds, the traveltime pairs are rejected. For the
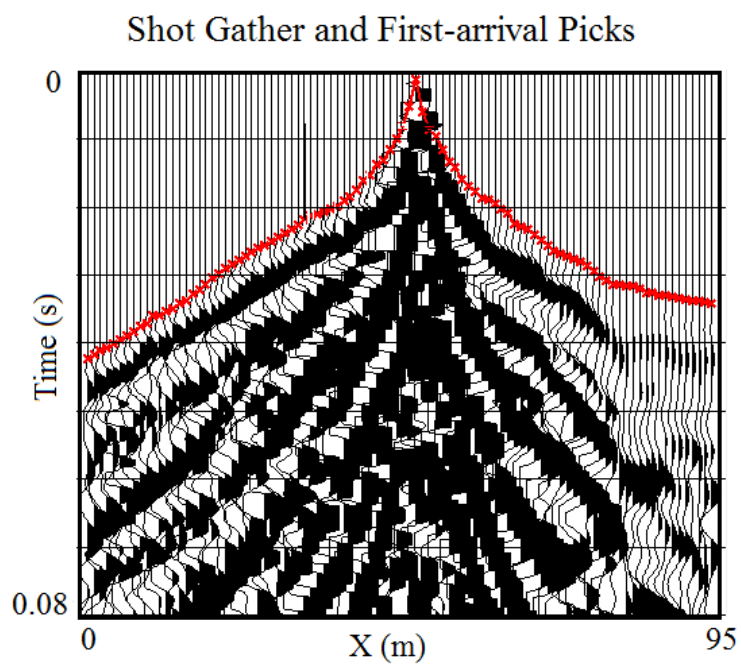
Figure 2.4. A common shot gather from 2-D Washington fault data set and first-arrival traveltime picks are denoted by the red star.

3-D data, 29,750 traveltime picks are rejected by failing the reciprocity test. The remaining traveltimes are inverted using the SIRT algorithm described in Section 2.2.1.

2.2.3   Smoothing Filter

Due to irregular raypath coverage in some parts of the velocity model, a rectangular smoothing filter is applied after each iteration in the inversion process (Nemeth et al., 1997). Table 2.2 gives a listing of smoothing schedules for the synthetic data and field data in this paper. The reconstructed velocity model is initially smoothed with a $20 \times 10 \times 10$ smoothing filter. After six iterations the smoothing filter size is halved, which results in a better spatial resolution. The final smoothing filter is iteratively reduced to a volume of $4 \times 2 \times 2$.

2.3   2-D CDP Reflection Processing

The goal of common depth point (CDP) reflection processing is to transform the seismic reflection data into an approximate reflectivity image of the subsurface. Because near-surface scattering, statics, and surface waves are dominant in the shallow seismic data, the following processing flow (Figure 2.5) is required to obtain reflectivity images (Yilmaz, 1987).

2.3.1   Data Sorting and Geometry Defining

The first step in CDP data processing is to convert the data format from Bison seismograph format to SEG-Y format so processing can be performed with ProMAX. Then the survey geometry is defined according to the field survey, including the shot and receiver locations, shot and receiver offsets, CDP locations, and other known parameters that affect the data processing.

2.3.2   Elevation Statics

The statics problem is defined to be static time shifts introduced into the traces by, e.g., near-surface velocity anomalies and/or topography. These time shifts distort the true geometry of deep reflectors. For the Washington experiment, large static time shifts are introduced by the large elevation changes in the topography. Thus, an elevation statics correction is applied to the data, so that the data appear to have been collected on a flat datum plane. The final datum elevation is the same as the highest topographic point, and the replacement velocity is 500 m/s for correcting the traces to the new datum.

Table 2.2. Smoothing schedule for synthetic and field data.

Seismic surveys	2-D synthetic data	3-D synthetic data	2-D field data	3-D field data
Grid size	0.5 m	0.5 m	0.5 m	0.5 m
Number of unknowns	4,800	72,000	4,800	72,000
Number of traveltimes	3,200	115,200	2,687	85,450
Smoothing size 1	20×10	$20 \times 10 \times 10$	20×10	$20 \times 10 \times 10$
Smoothing size 2	12×6	$12 \times 6 \times 6$	12×6	$12 \times 6 \times 6$
Smoothing size 3	8×4	$8 \times 4 \times 4$	8×4	$8 \times 4 \times 4$
Smoothing size 4	4×2	$4 \times 2 \times 2$	4×2	$4 \times 2 \times 2$
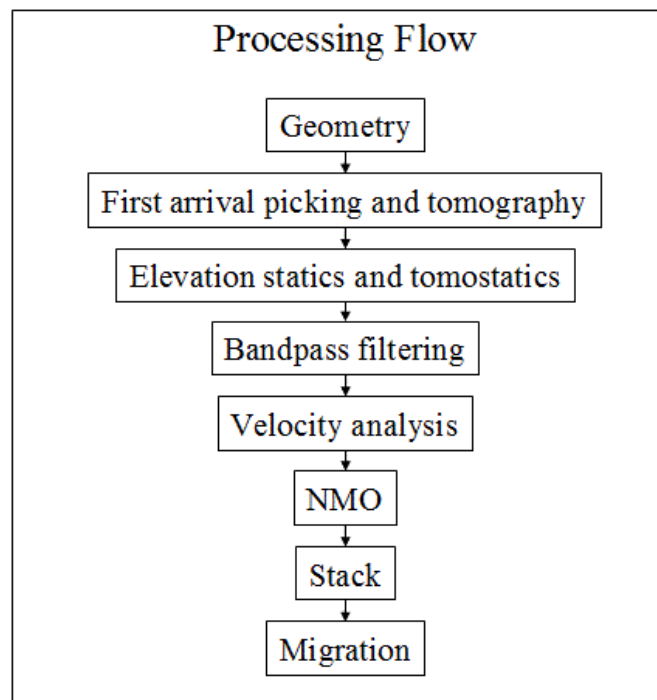
Figure 2.5. Flowchart for reflection processing of the 2-D Washington fault data set. Here, AGC = automatic gain control, NMO = normal moveout correction, CMP = common midpoint.

2.3.3 Bandpass Filter

To remove the low-frequency noise (such as surface waves), 40-200 Hz bandpass filtering was applied to the traces. The low-frequency surface waves are mostly suppressed by this filter.

2.3.4 NMO and Stacked Section

The seismic data are sorted into 190 common midpoint gathers (CMG) with 0.5 meter spacing. Two or three near-zero-offset traces of each CMG were selected for stacking.

2.3.5 Poststack Migration

In order to move dipping reflectors into their correct positions and collapse diffractions, poststack migration was applied to the stacked data, where the maximum dip angle is limited to no more than 30 degrees. The migration method selected was Kirchhoff migration.

CHAPTER 3

NUMERICAL RESULTS FOR SYNTHETIC
DATA

The migration and tomographic images for synthetic data are presented in this chapter. The results suggest that the faults and LVZs can be clearly imaged by seismic methods, and 3-D tomograms are more accurate and have fewer artifacts than 2-D tomograms in delineating fault structures.

3.1   Traveltime Tomography of Synthetic Data

To understand the sensitivity of the tomography method in delineating fault structures, both 2-D and 3-D synthetic tests are carried out. The input model is a 3-D fault model, and has the same dimension as the area investigated with the 3-D Washington fault experiment. The model was constructed by defining the background velocity to be similar to that of the actual 3-D Washington fault tomogram. The velocity at the ground surface is defined to be 500 m/s and the vertical velocity gradient is assigned as 110 m/s, and the depth of bedrock is about 15 m below the surface, with the velocity 2,400 m/s. There is no variation of velocity in the Y direction. An X-Z velocity slice of the fault model is shown in Figure 3.1(a). The source and receiver geometry for the synthetic test are identical to that of the 3-D Washington fault experiment, shown in Figure 2.3. Approximately 115,200 first-arrival traveltimes are generated by solving the 3-D eikonal equation with a finite-difference method (Qin et al. 1992), and the traveltimes taken from the first source line and receiver line (Y=0 m) are used for 2-D traveltime inversion. Table 3.1 summarizes the model and acquisition parameters for the synthetic tests.

The first-arrival traveltimes are inverted to obtain the P-wave velocity distribution, and a gradient model with velocities ranging from 500 m/s at shallow depths to 2,400 m/s at depth are used for the initial model. The reconstructed velocity model is initially smoothed with a 20 $\times$ 10 $\times$ 10 smoothing filter, and the smoothing filter is iteratively reduced to a volume of 4 $\times$ 2 $\times$ 2.
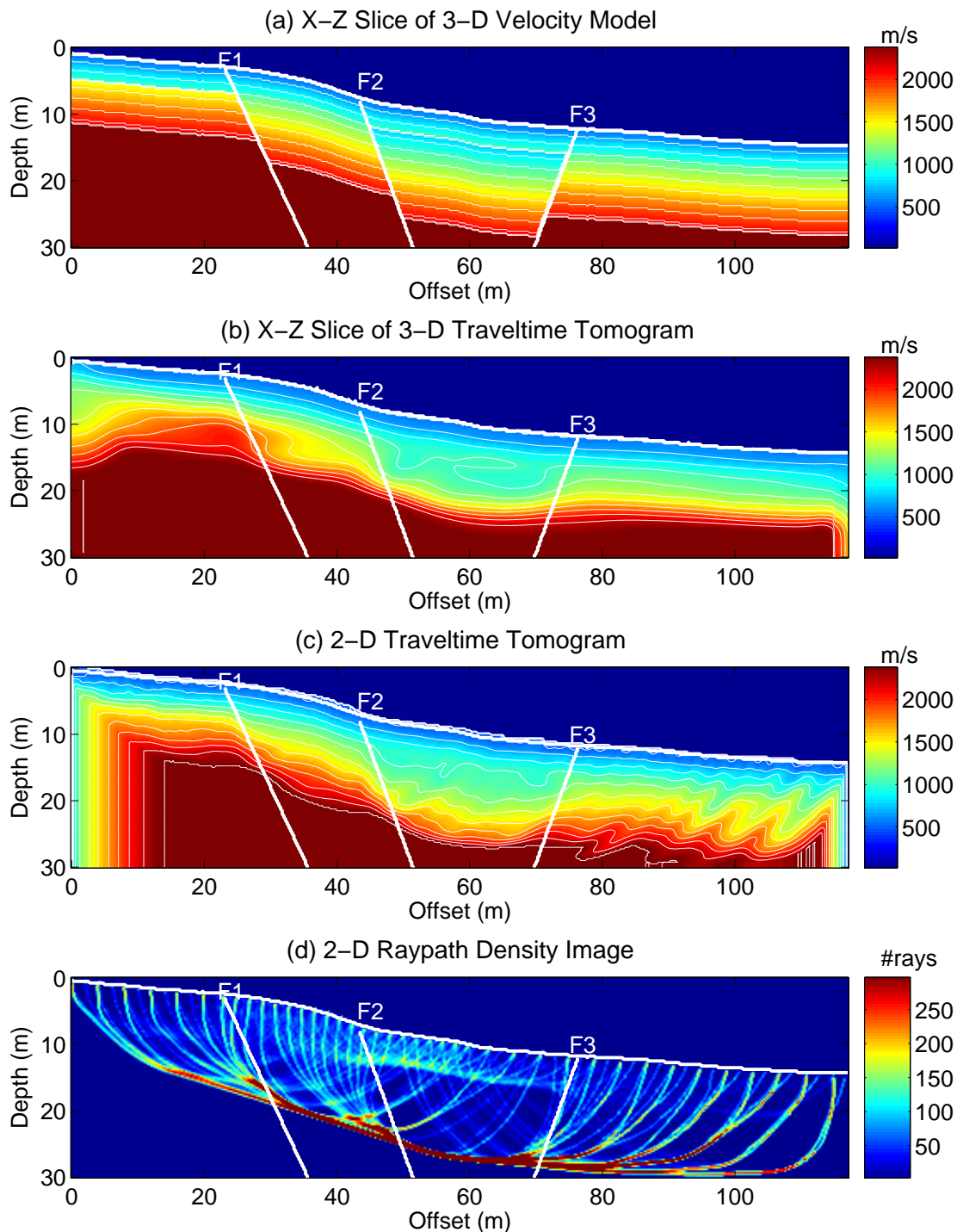
Figure 3.1. Results of 2-D and 3-D traveltime tomography test. (a): an X-Z slice of the linear gradient velocity model with 3 normal faults. (b): an X-Z slice of the 3-D tomogram along the first receiver line (Y = 0 m). (c): 2-D traveltime tomogram along the first receiver line (Y = 0 m). (d): raypath density image obtained from 2-D traveltime inversion.

Table 3.1. Model and acquisition parameters for the synthetic tests.

Surveys	2-D	3-D
Model size	117 m × 30 m	117 m × 7.5 m × 30 m
Grid size	0.5 m	0.5 m
Number of shots	40	240
Number of receivers	80	480
Shot/receiver spacing	Shown in Figure 2.3	Shown in Figure 2.3
Survey length	117 m	117 m
Number of traveltimes	3,200	115,200

A comparison between the 2-D and 3-D tomograms is shown in Figures 3.1(b) and Figure 3.1(c). Both of the tomograms are along the first receiver line (Y=0 m), and the images obtained from 2-D and 3-D tomography are comparable at low wavenumbers. The fault surfaces in the model are characterized by a smooth down drop of the velocity contours in both of the tomograms. This is not surprising, since previous studies (Buddenseik, et al., 2007) empirically showed that the tomogram is a smoothed version of the actual velocity, where faults are characterized by a smooth downdrop in tomographic velocities. Another observation is that the 3-D tomogram seems to have fewer artifacts than the 2-D tomogram. This should not be too surprising, because rays in the the 3-D survey are characterized by a greater diversity of ray angles, which leads to better model resolution. In addition, the ratio of unknowns to traveltime equations (shown in Table 2.2) is smaller for the 3-D tomogram and suggests a more stable and overdetermined solution. In Figure 3.2, the velocity and gradient profiles at X=26 m (Fault 1), X=48 m (Fault 2) and X=74 m (Fault 3) are compared. The faults are identified as large positive gradient values of velocity, and the fault structures delineated in the 3-D tomogram are more accurate than those in the 2-D tomograms. Figure 3.1(d) depicts the 2-D raypath density image, which displays the number of rays visiting each cell of the tomogram. For the normal-slip fault (F1, F2 and F3), the rays focus near the fault plane, which results in fewer raypaths visiting the hanging wall side, and the LVZ (48 m<X<75 m) has lower raypath coverage than other regions.

To assess the convergence of the iterative solution, a plot of RMS traveltime residual vs. iteration number is shown in Figure 3.3. It demonstrates that the iterative solutions converge within ten iterations. The final traveltime residual is about 0.3 ms, which is close to 0, since no picking errors are added.

3.2 CDP Reflection Processing of the Synthetic Data

To locate the fault positions, CDP reflection processing is carried out. The velocity model is the same as the 2-D model in Section 3.1, and Figure 3.4(a) shows the reflectivity image computed from the velocity model. To make the processing simple, the sources and receivers are distributed evenly at 1 m spacing for a total line length of 117 m. A 2-4 finite-difference solution to the acoustic wave equation is used to generate the zero-offset seismograms, and Table 3.2 gives the model and acquisition parameters for the synthetic tests. Figure 3.4(b) shows the stacked seismic section with the horizontal axis in offset and the vertical axis in time. Figures 3.4(c) and 3.4(d) show the migration images using the true velocity and the velocity obtained from the tomogram, respectively. Although there
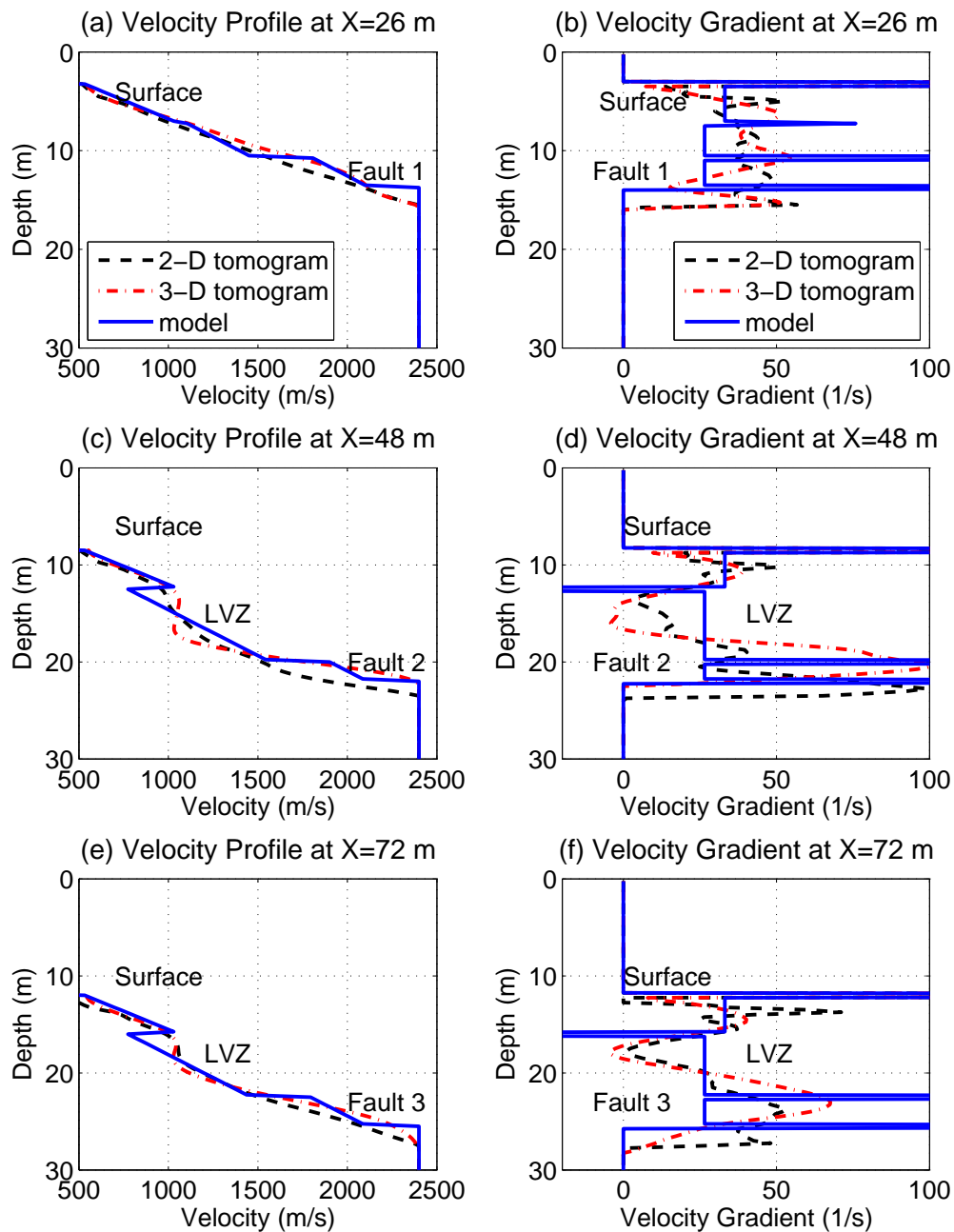
Figure 3.2. Velocity and gradient profile comparison at 3 different locations for the synthetic test. Left panels are the velocity profiles, and right panels are the velocity gradient profiles. In the velocity gradient profiles, the faults are identified by large positive gradient values and LVZs are identified by large negative gradient values.
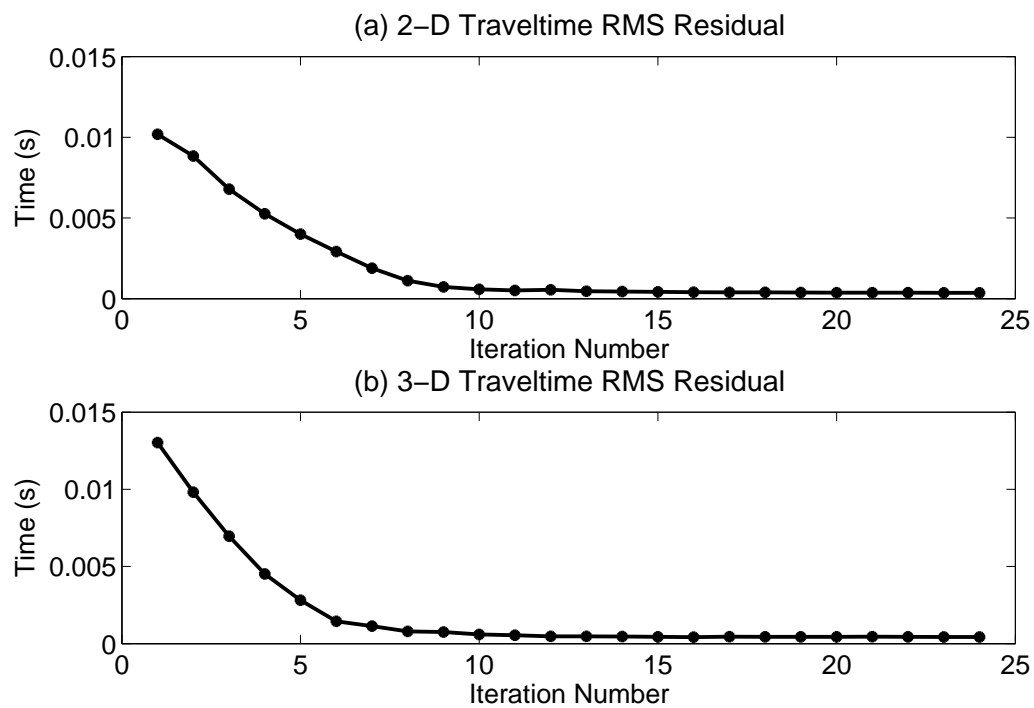
Figure 3.3. 2-D and 3-D RMS traveltime residual vs. iteration number. The iterative solutions converge after about ten iterations. The final traveltime residual is about 0.3 ms, which is close to 0, since no picking errors are added.
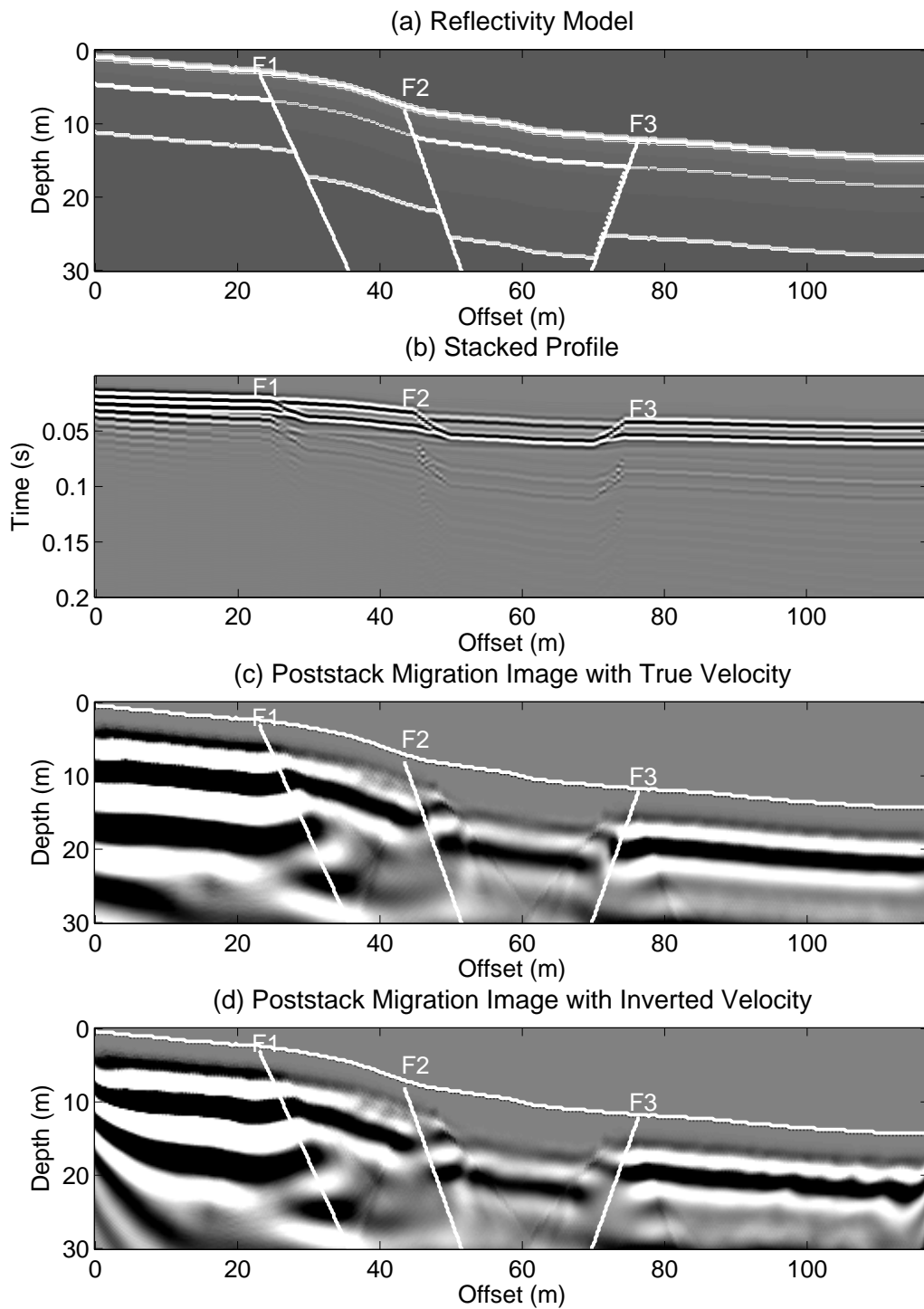
Figure 3.4. Stack and migration images. (a): the reflectivity image computed from the velocity model. (b): the stacked seismic section with the horizontal axis in offset and the vertical axis in time. (c): the migration images using the true velocity. (d): the migration images using the inverted velocity from tomography.

Table 3.2. Model and acquisition parameters for the CDP reflection processing.

Model size	117 m × 30 m
Grid size	0.25 m
Number of shots	118
Number of receivers	118
Shot/receiver spacing	1 m
Source	100 Hz Ricker wavelet
Recording length	0.2 s
Sampling interval	0.02 ms

are some artifacts in the migration image using the tomographic velocity, where the layers around X<15 m are tilted and the layers around X>90 m undulate, the fault locations are clearly identified with the correct dip angles.

CHAPTER 4

NUMERICAL RESULTS FOR FIELD DATA

The 2-D and 3-D tomographic results and the 2-D migration images are computed for data recorded from the Washington fault experiment and analyzed in this chapter. My interpretation suggests that there are four faults and two large LVZs. These LVZs are likely to be colluvial wedge packages, as they appear to be associated with the faulting.
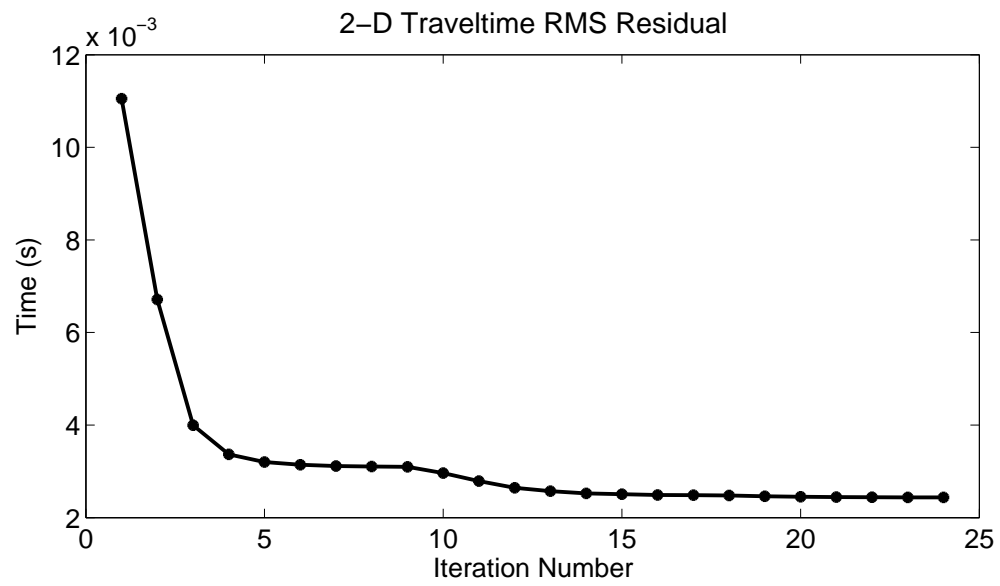
4.1   Tomographic Results

4.1.1   2-D Tomographic Results

One 2-D survey line is taken from the original 3-D data. The first-arrival traveltimes are picked from 3,200 traces, where 513 traveltime picks were rejected because they did not satisfy the reciprocity condition within a tolerance of 3 milliseconds. The remaining traveltimes are inverted to obtain the P-wave velocity distribution. Figure 4.1(a) depicts the velocity tomogram presented as contours of seismic velocity in depth along the profile, and Figure 4.1(b) displays the raypath density through each cell in the tomogram. Based on the synthetic tests in Chapter 3, two criteria are used to identify a fault in the tomogram: (1) Focusing of rays in the raypath density image (the fault is not exactly located at the greatest raypath density area, but is located at the low-density side near the plane (Figure 3.1). (2) A sharp change in the velocity gradient (Figure 3.2). Combining the tomogram, velocity gradient profile, raypath density distribution, and migration image (discussed in Section 4.2) together, four faults are interpreted, numbered from F1 to F4. Four LVZs are outlined with ellipses in the traveltime tomogram. In the raypath density, the LVZs correspond to the zones of low raypath density, marked with ellipses as well. A plot of RMS traveltime residual vs. iteration number is shown in Figure 4.2. The final RMS traveltime residual is about 2.4 ms, which is slightly smaller than the estimated picking error of 3 ms.
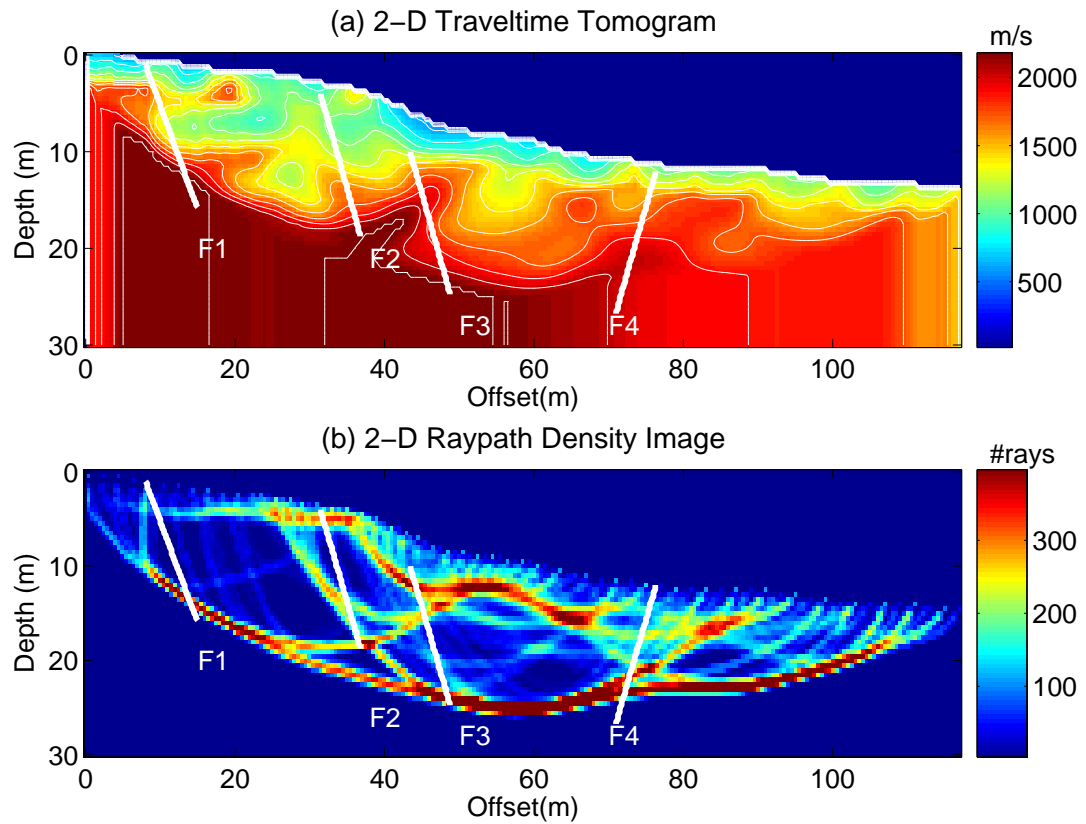
Figure 4.1. 2-D traveltime tomogram and raypath density image. (a): the 2-D traveltime tomogram with the fault interpretation. (b): the raypath density image.

Figure 4.2. RMS traveltime residual vs. iteration number. The solution converges after about twenty iterations, and final RMS traveltime residual is about 2.4 ms.

4.1.2 3-D Tomographic Results

The first-arrival traveltimes are picked from 115,200 traces in the original data set, where 29,750 traveltime picks are rejected because they failed the reciprocity test or were deemed unpickable. The 3-D velocity tomogram is inverted from these picks and is shown in Figure 4.3. Four X-Z slices spaced every 2 m along the Y direction are shown in Figure 4.4. This tomogram clearly delineates three large LVZs. The one denoted as LVZ1 is located at X=20∼35 m, LVZ2 is located at about X=50∼65 m, and LVZ3 is located along the near surface at X=35∼65 m. All of the LVZs are parallel to the fault scarp. The main fault, F3, interpreted from the migration image and the raypath density image, is located at the offset of 45 m, and suggests that LVZ2 is possibly the colluvial wedge generated by surface rupture events on the Washington fault. The LVZ3 is possibly another colluvial wedge package and is the youngest of the LVZs. Comparing the 2-D tomogram with the 3-D tomogram, both have similar structures at low wavenumbers; but, the 3-D tomogram has fewer artifacts than the 2-D tomogram. To access the accuracy of the predicted traveltimes, a plot of RMS traveltime residual is shown in Figure 4.5. The final RMS traveltime residual is about 3.2 ms, which is almost the same as the estimated picking error of 3 ms.

4.2 Reflection Results

The 3-D Washington fault data have less observable reflection energy seen in the seismogram. This is because only a 10-lb sledgehammer was used in the 3-D experiment, compared to the 16-lb sledgehammer in the 2-D experiment; and the 2-D experiment had a shorter survey length. Here, only the 2-D seismic data are used for reflection stacking. The common shot gathers (CSGs) are sorted into 190 common midpoint gathers (CMGs) with 0.5 m spacing, and two or three near-zero-offset traces of each CMG were selected for stacking.

Figure 4.6 shows the stacked seismic section with the horizontal axis in offset and the vertical axis in time. It shows more than two shallow horizons, which are mostly continuous, except for the region around X=14 m. From the stacked profile, it is difficult to determine the locations of the fault planes. To delineate the fault structures clearly, the stacked data are migrated. Figure 4.7 shows the final migration image, and using the migration images of the synthetic data as a guide, the layered horizons are discontinuous at the fault plane. Here, four faults (F1∼F4) are interpreted, combined with the tomogram and raypath density image, where F3 is possibly the main fault, and F4 is the antithetic fault. The dip angles of the four faults are estimated from the migration image to be about 80+/-10 degrees. This
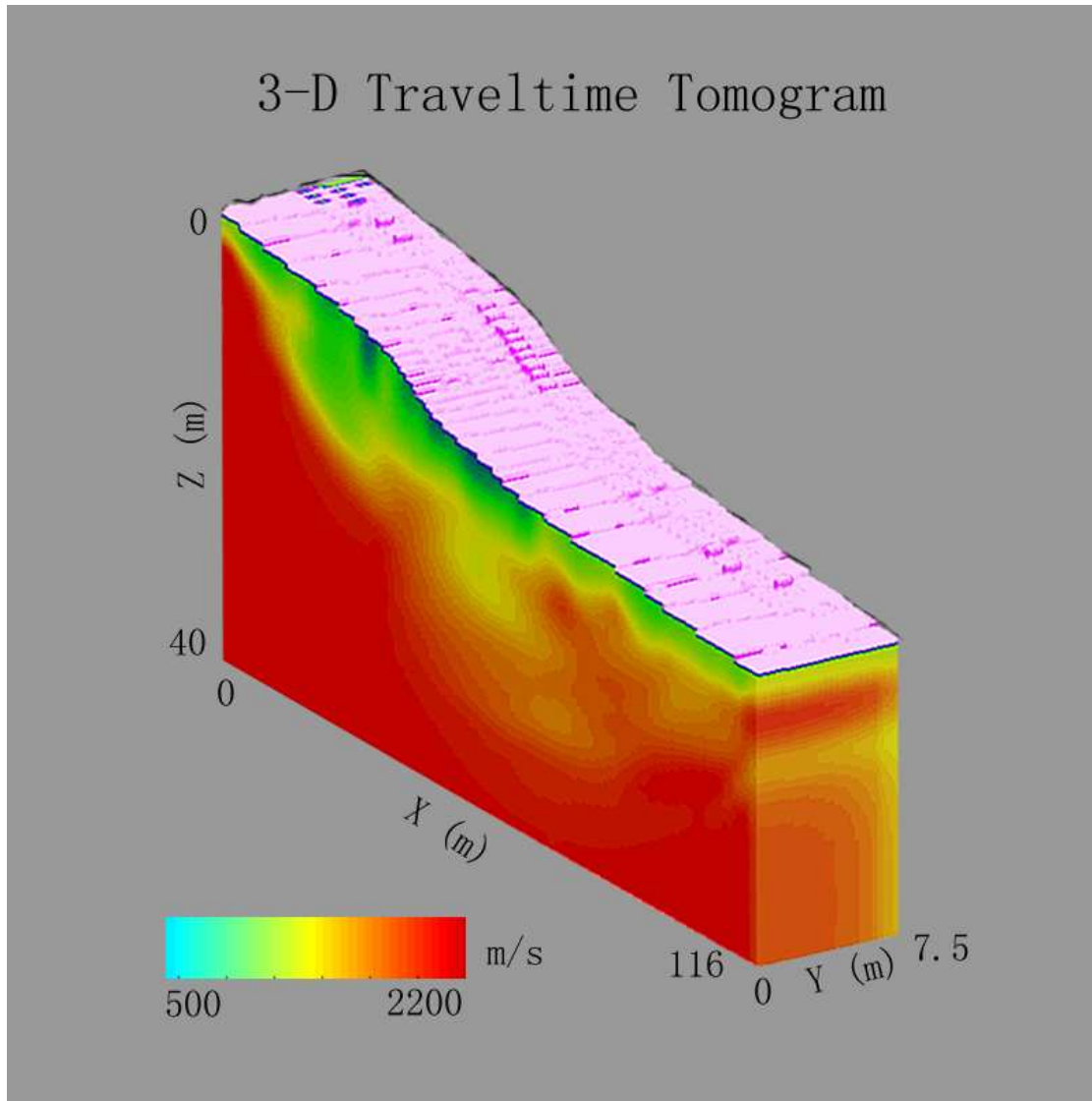
Figure 4.3. The volume of the 3-D velocity tomogram. Two large LVZs are clearly delineated in the tomogram.
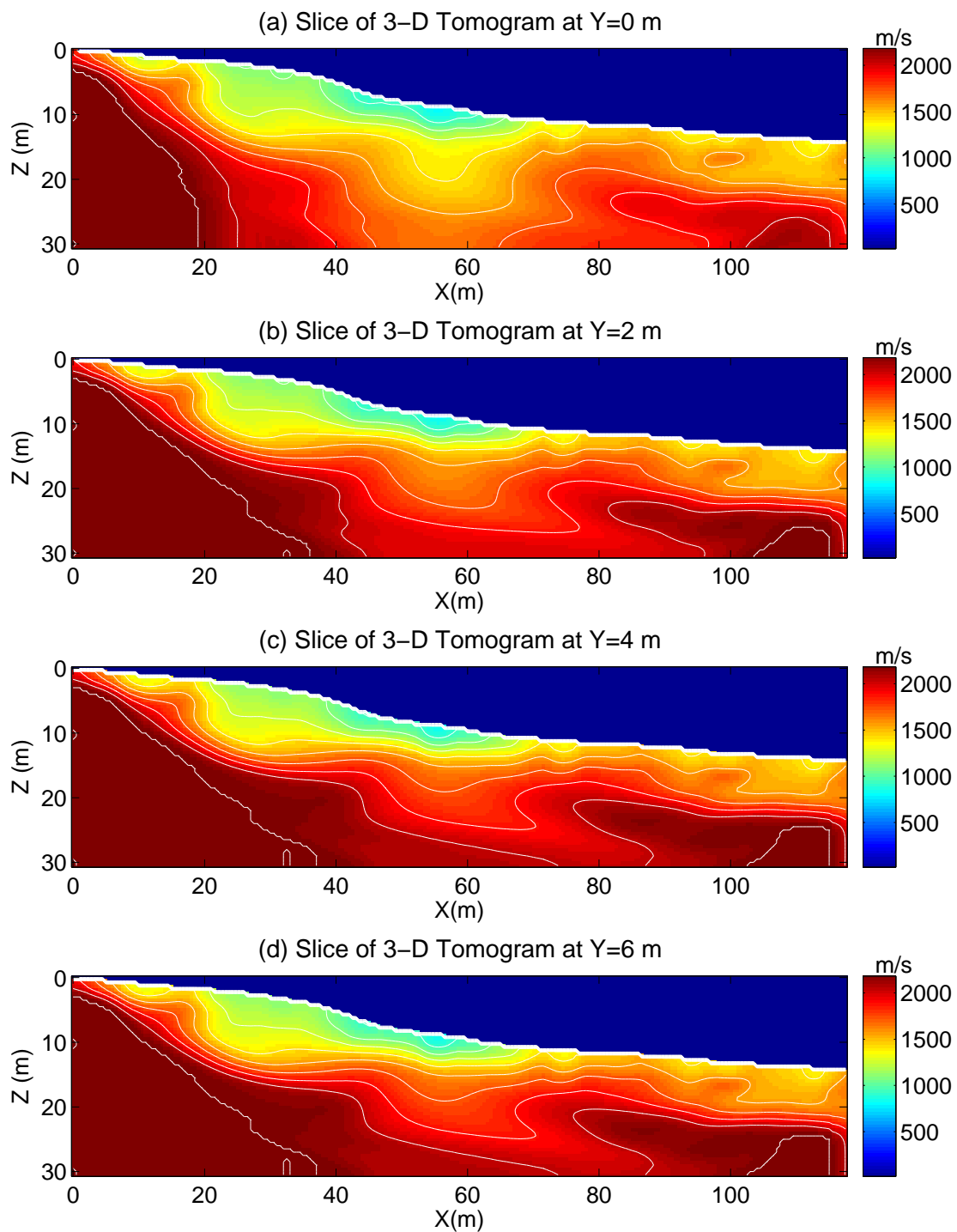
Figure 4.4. X-Z slice of 3-D velocity tomogram. (a): slice at Y = 0 m. (b): slice at Y = 2 m. (c): slice at Y = 4 m. (d): slice at Y = 6 m.
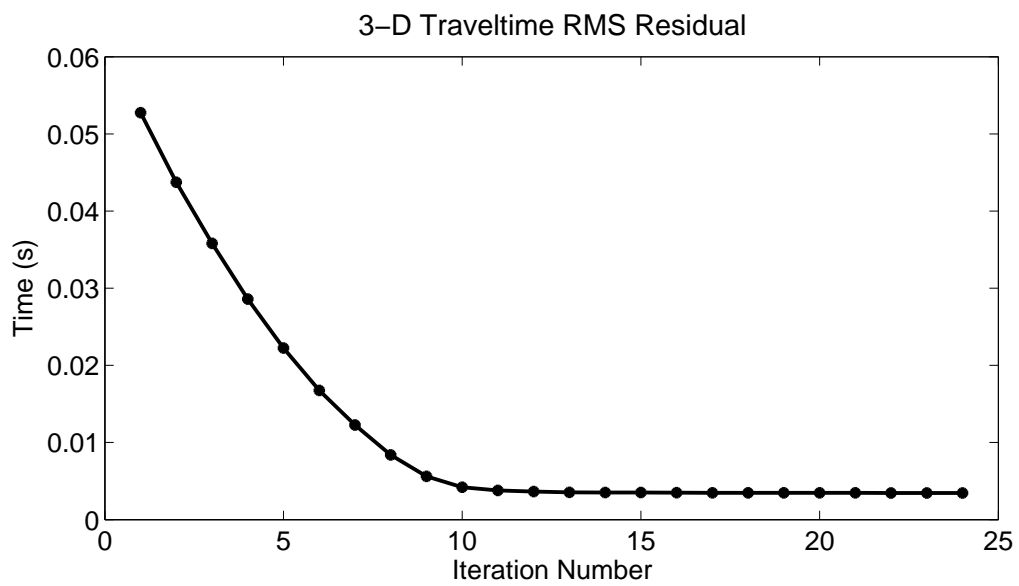
Figure 4.5. RMS traveltime residual vs. iteration number. The solution converges after about fifteen iterations, and the final traveltime residual is about 3.2 ms.

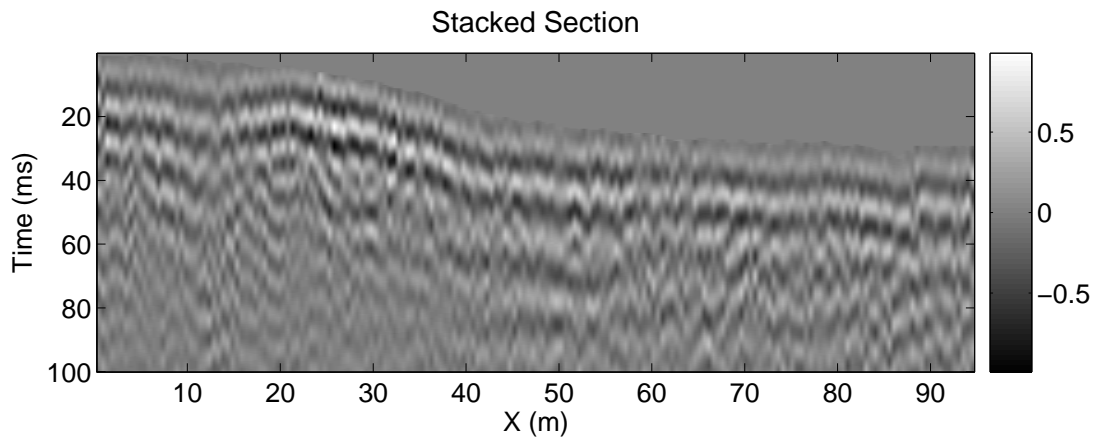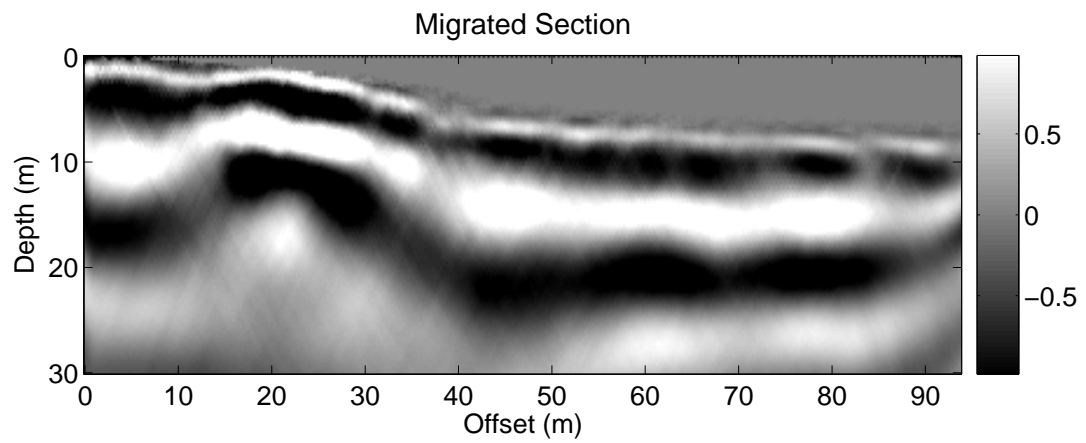**Figure 4.6**. Stacked profile of 2-D seismic data.

Figure 4.7. Migration image of 2-D seismic data.

is consistent with the description of the Washington fault by Higgins (1998).

4.3   Interpretations

Figure 4.8 presents a summary of the tomographic results and the migration image. From the 2-D and 3-D traveltime tomograms and 2-D migration images, we can identify the following features:

(1) Three LVZs (LVZ1, LVZ2 and LVZ3) have been imaged with both 2-D and 3-D traveltime tomography. To establish their identity, age, and the estimated frequency of past earthquake occurrence, a much cheaper alternative than trenching is to drill a well over the areas (20 m< X <35 m and 50 m< X <65 m).

(2) F3 is likely to be the main fault, which is consistent with geomorphology data, and F4 is a possible antithetic fault.

(3) The depth of the bedrock is estimated to be about 15 m, with the velocity larger than 2200 m/s.

(4) The four faults have an apparent dip of approximately 70-80 degrees.

(5) From the 3-D tomogram, the thickness of the LVZ1 and LVZ2 is about 5 m, and the thickness of LVZ3 is about 2 m.

Four faults and three LVZs are interpreted in Figure 4.9 finally. Table 4.1 summarizes the features interpreted from Figure 4.8 and Figure 4.9. The thickness of LVZs can be considered as an approximation of the fault vertical slip. Combining the fault slip rate from paleoseismic data with the fault slip inferred by tomography, the age of the fault can be speculatively estimated. Earth Sciences Associates (1982) state that the slip rates for the Washington fault are 0.003 mm/yr for the past 1.5 kyr, and a minimum slip rate of 0.03~0.12 mm/yr for the past 10 to 25 kyr. If these estimates are correct, then I estimate that the fault activity started later than 16 kyr.
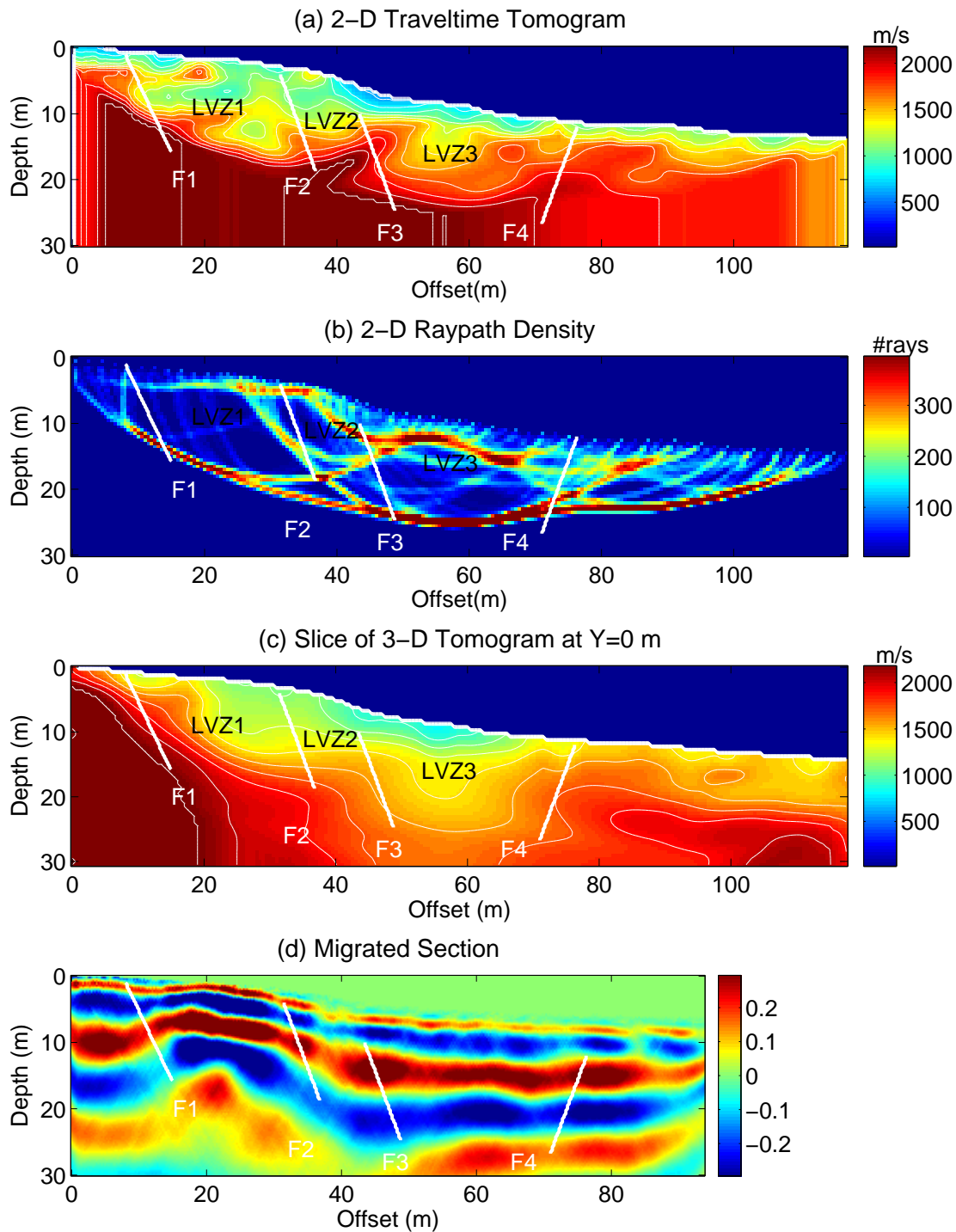
Figure 4.8. Summary of tomographic results and migration image, and interpretation.
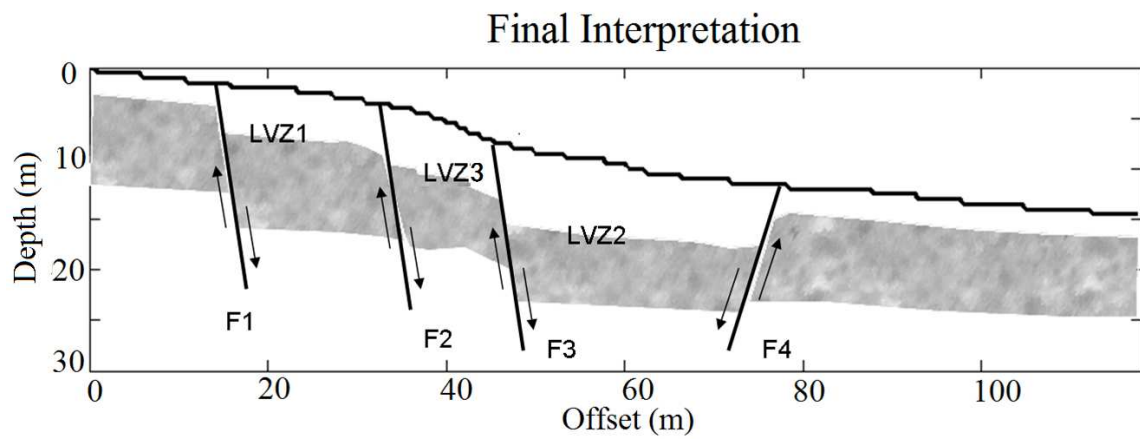
Figure 4.9. Final interpretation.

Table 4.1. List of the features from the interpretation of Figures 4.8 and 4.9. The letters 'h', 'd', and 'w' indicate the thickness, depth and width of the LVZs, respectively.

	Location	Features
F1	15 m	80 degrees
F2	35 m	80 degrees
F3	42 m	80 degrees (main fault)
F4	76 m	70 degrees (antithetic fault)
LVZ1	20~35 m	h=5 m, d=3 m, w=15 m
LVZ2	50~65 m	h=5 m, d=7 m, w=15 m
LVZ3	35~65 m	h=2 m, d=0 m, w=30 m

CHAPTER 5

CONCLUSIONS

Seismic experiments were conducted across the Washington fault with the goal of imaging the shape and location of faults and colluvial wedges. The 3-D data consisted of 115,200 traces, of which 85,450 traveltimes were picked and inverted to estimate the 3-D velocity structure of the Washington fault over a volume of 116 m x 7.5 m x 30 m. Reflectivity images from the 2-D seismic data provided information on the fault zone that was used, in conjunction with information from the 3-D tomogram, to estimate fault and colluvial wedge package locations associated with prehistoric earthquakes along the Washington fault.

The results of processing the 2-D and 3-D seismic surveys over the Washington fault show consistent images that appear to be faults and LVZs to a depth of about 30 m. From the 2-D and 3-D traveltime tomograms and the 2-D migration images, we can identify the following consistent features:

(1) Three LVZs (LVZ1, LVZ2 and LVZ3) are imaged with both 2-D and 3-D traveltime tomography.

(2) F3 is likely to be the main fault, which is consistent with geomorphology data, and F4 is the possible antithetic fault.

(3) The depth of the bedrock is estimated to be about 15 m, with the velocity larger than 2200 m/s.

(4) The four faults have an apparent dip of approximately 70-80 degrees.

(5) From the 3-D tomogram, the thickness of the LVZ1 and LVZ2 is about 5 m, and the thickness of LVZ3 is about 2 m.

(6) Combining the fault slip rate from paleoseismic data with the fault slip inferred by tomography, the age of the fault is estimated to be younger than 16 kyr.

I have demonstrated that seismic tomographic images can reveal the shape and depth of LVZs, which are possibly colluvial wedge packages associated with normal-fault earthquakes. This result was used by UGS personnels to optimally design a trenching survey over this area. A much cheaper alternative is to drill into the LVZs to establish their identity and age,

and to estimate the frequency of past earthquake occurrence. A future task is to compare the tomogram with the trench log, and analyze the accuracy of my interpretation.

APPENDIX

3-D TRAVELTIME TOMOGRAPHY ALGORITHM

Traveltimes associated with direct and turning rays were inverted by a nonlinear inversion method, where the traveltimes were computed by a finite-difference solution to the eikonal equation (Qin et al., 1992). The model velocities are updated each iteration by a simultaneous iterative reconstruction technique (SIRT) (Gilbert, 1972). In this scheme the data misfit function is defined as:

$$\epsilon = \frac{1}{2} \sum_i (t_i^{obs} - t_i^{cal})^2, \tag{A.1}$$

where the summation is over the i_{th} raypaths, t_i^{obs} is the associated first-arrival traveltime pick, and t_i^{cal} is the calculated traveltime. The gradient of the misfit function is given by:

$$\gamma_j = \frac{\delta\epsilon}{\delta s_j} = \sum_i \delta t_i \frac{\delta t_i}{\delta s_j}, \tag{A.2}$$

where δt_i is the traveltime residual and δs_j is the slowness in the jth cell. Equation A.2 can be written as:

$$\gamma_j = \sum \delta t_i l_{ij} \approx l \sum \delta t_i, \tag{A.3}$$

where l_{ij} is the segment length of the i_{th} ray that visits the j_{th} cell, and l is the width of a square cell. By assuming that all the ray segments within a cell are of equal length, the model updating direction is given by the normalized formula:

$$\gamma_j = -\frac{1}{N_j} \sum_{i=1} \delta t_i, \tag{A.4}$$

where γ_j is the negative gradient of the misfit function in the j_{th} cell, N_j is the number of rays that visit the j_{th} cell, δt_i is the traveltime residual and the summation is over the indices associated with raypaths that visit the j_{th} cell.

If a cell has no raypaths passing through, i.e., $N_j = 0$, it is assigned the same gradient value as the cell just above it. This is called gradient downward extrapolation, because it extends the gradient field downward from the deepest point where rays can reach for a given survey geometry. This technique is based on the fact that we do not have information below the maximum depth of ray penetration, so we assume a downward continuation of known velocities. This point must be kept in mind when interpreting an image, because the edges of the image will display vertical striping associated with shallow ray penetration.

REFERENCES

[1] Aldridge, D. F., and D. W. Oldenburg, 1993, Two-dimensional tomographic inversion with finite-difference traveltimes: Journal of Seismic Exploration, v. 2, p. 257-274.

[2] Ammon, C. J., and J. E. Vidale, 1993, Tomography without rays: Seismological Society of America Bulletin, v. 83, p. 509-528.

[3] Arabasz, W. J., J. C. Pechmann, and E. D. Brown, 1992, Observational seismology and the evaluation of earthquake hazards and risk in the Wasatch front area, Utah: U.S. Geological Survey Professional Paper, v. 1500-A-J, p. D1-D36.

[4] Buddensiek, M. L., J. Sheng, T. Crosby, G. T. Schuster, R. L. Bruhn, and R. He, 2007, Colluvial wedge imaging using traveltime and waveform tomography along the Wasatch fault near Mapleton, Utah: Geophys. J. Int., v. 162, p. 246-277.

[5] Christenson, G. E., 2004, Improving our understanding of earthquake hazards in Utah: UGS Survey Notes, v. 4, p. 122-156.

[6] Gilbert, P., 1972, Iterative methods for the three-dimensional reconstruction of an object from projections: J. Theor. Biol., v. 36, p. 105-117.

[7] Higgins, J. M., 1998, Interim geologic map of the Washington Dome quadrangle, Washington County, Utah: Utah Geological Survey Open-File Report, v. 363, 128 p., scale 1:24,000.

[8] Lutter, D., R. Nowack, and L. Braile, 1990, Seismic imaging of upper crustal structure using travel times from the Passcal Ouachita experiment: J. Geohys. Res., v. 95, p. 4621-4631.

[9] Morey, D., and G. T. Schuster, 1999, Paleoseismicity of the Oquirrh fault, Utah from shallow seismic tomography: Geophys. J. Int., v. 138, p. 25-35.

[10] Nemeth, T., E. Normark, and F. Qin, 1997, Dynamic smoothing in cross-well traveltime tomography: Geophysics, v. 62, p. 168-176.

[11] Nolet, G., 1987, Seismic tomography: with applications in global seismology and exploration geophysics: Dordrecht, Holland, Reidel Publishing Co., 265 p.

[12] Pechmann, J. C., and W. J. Arabasz, 1995, The problem of the random earthquake in seismic hazard analysis: Wasatch front region, Utah: Utah Geological Association Publication, v. 24, p. 77-93.

[13] Qin, F., Y. Luo, K. B. Olsen, W. Cai, and G. T. Schuster, 1992, Finite-difference solution of the eikonal equation along expanding wavefronts: Geophysics, v. 57, p. 478-487.

[14] Sheley, D., T. Crosby, M. Zhou, J. Giacoma, J. Yu, R. He, and G. T. Schuster, 2003, Two dimensional seismic trenching of colluvial wedges and faults: Tectonophysics, v. 368, p. 51-69.

[15] Yilmaz, O., 1987, Seismic data processing: Tulsa, OK, Society of Exploration Geophysicists, 382 p.